Nanoscale

Hollow silica-copper-carbon anodes using copper metal-organic frameworks as skeletons

Zixu Sun[†], Fengxia Xin[†], Can Cao[‡], Chongchong Zhao[†], Cai Shen[†], Wei-Qiang Han[†,*]

[†]*Ningbo Institute of Materials Technology & Engineering, Chinese Academy of Sciences, Ningbo 315201, P. R. China*

[‡]*Department of Materials Science and Engineering, Zhejiang University, Hangzhou 310027, P. R. China*

*Correspondence and requests for materials should be addressed to W.Q.H. *e-mail:*

hanweiqiang@nimte.ac.cn

KEYWORDS: Cu-MOF, silica-copper-carbon, skeleton, anode material, hollow structure

ABSTRACT

Hollow silica-copper-carbon (H-SCC) nanocomposites are first synthesized using copper metal-organic frameworks as skeletons to form Cu-MOF@SiO$_2$ and then subsequent heat treatment. In the composites, the hollow structure and the void space from the collapse of the MOF skeleton can accommodate the huge volume change, buffer the mechanical stress caused by lithium ions insertion/extraction and maintain the structural integrity of the electrode and a long cycling stability. The ultrafine copper with uniform size of around 5 nm and carbon with homogeneous distribution from the decomposition of the MOF skeleton can not only enhance the

electrical conductivity of the composite and preserve the structural and interfacial stabilization, but also suppress the aggregation of silica nanoparticles and cushion the volume change. In consequence, the resulting material as an anode for lithium-ion batteries (LIBs) delivers a reversible capacity of 495 mA h g^{-1} after 400 cycles at a current density of 500 mA g^{-1}. The synthetic method presented in this paper is provided a facile and low-cost strategy for the large-scale production of hollow silica/copper/carbon nanocomposite as an anode in LIBs.

INTRODUCTION

Lithium-ion batteries (LIBs) with long cycle life, high capacity and high-rate performance are under extensive studies to meet the challenging requirements, such as portable electronic devices, electric vehicles, and stationary grid storage[1-4]. Silicon-based materials are promising candidates to replace currently graphite anodes because of their high theoretical specific capacity of 4200 mA h g^{-1}, which is 10 times higher than that of graphite (372 mA h g^{-1})[5]. However, silicon-based materials are seriously hindered by drastic volume changes during lithiation/delithiation process, resulting in pulverization of silicon nanoparticles and unstable solid electrolyte interface (SEI) film and rapid capacity decay[6-13]. Much attention has recently turned to SiO_2 as an alternative of Si for LIBs due to its high abundance, low working potential, and high theoretical specific capacity of 1965 mA h g^{-1}[14-17]. Also, compared to silicon-based materials, it undergoes much less volume change because of the irreversible products of silicate/LiO_2 during the first charge-discharge cycle, which can cushion the volume change and prevent the composite aggregation[16]. However, one of the most obstacles which hinder the practical application of SiO_2 as an anode for LIBs is its low intrinsic electrical conductivity, which can be improved by applying carbon coatings to enhance the electric conductivity of the electrode and also to buffer the volume change of SiO_2[7, 16, 18]. Cu dissolves easily in silicon-

based matrices and has superior conductivity and ductility[19-28]. It is electrochemically inactive, but it can form copper silicide intermetallic that can improve the electrical conductivity and the mechanical flexibility[29].

Metal-organic frameworks (MOFs) constructed by metal ions (clusters) and organic linkers are a new class of hybrid functional materials with large specific surface area and high porosities, and have wide applications in catalysis, drug delivery, photochemical and electrochemical[9, 30-34]. Recently there have been many reports of using MOFs as precursor materials or templates to synthesize active materials for LIBs, which exhibit excellent electrochemical performance. For example, porous spinel $Zn_xCo_{3-x}O_4$[35] and CuO hollow polyhedral material[32] have been synthesized for LIBs, showing potential application in commercial LIBs. Spindle-like mesoporous α-Fe_2O_3 anode material has been prepared from an iron-based MOF template and shows greatly improved electrochemical performance[36]. Nevertheless, to the best of our knowledge, there has been no report on the synthesis of hollow SiO_2 anode material for LIBs using MOFs as templates.

Herein for the first time we report a simple and scalable and low-cost synthesis of hollow SiO_2/Cu/C (H-SCC) nanocomposite with ultrafine Cu nanoparticles embedded in the amorphous SiO_2 matrices via the conversion of the Cu-MOF@SiO_2, which has the features of electrically and mechanically robust structure. This composite shows several advantages, as follows: (1) the hollow structure and the void space from the structure collapse of the MOF skeleton, which can accommodate the huge volume change and buffer the mechanical stress caused by lithium ions insertion/extraction and maintain the structural integrity of the electrode and a long cycling stability; (2) the ultrafine copper and carbon from the decomposition of the MOF skeleton, which can not only enhance the electrical conductivity of the composite and preserve the structural and

3

interfacial stabilization, but also can suppress the aggregation of silica nanoparticles and cushion the volume change; (3) the irreversible Li_2O and lithium silicate materials, which irreversibly produce from the first discharge process and also can buffer the volume change upon cycling; and (4) moreover, the synthetic method presented in this paper may provide a facile strategy for the large-scale production of hollow silica/copper/carbon composite. When it is evaluated as an anode material for LIBs, the as-prepared H-SCC nanocomposite exhibits electrochemical performance of relative higher capacity with stable stability.

Experimental details

Reagents and Chemicals. Ethanol (C_2H_6O, AR) and p-Phthalic acid ($C_8H_6O_4$) were purchased from Sinopharm Chemical Reagent Co. Ltd. Copper sulfate pentahydrate ($CuSO_4 \cdot 5H_2O$), sodium hydroxide (NaOH, AR), ammonia solution ($NH_3 \cdot H_2O$, AR, 25-28%), and tetraethyl orthosilicate (TEOS, metals basis) were purchased from Aladdin Chemistry Co. Ltd. All chemicals were used as received without further purification.

Synthesis of Cu-MOF. In a typical procedure, 0.012 mol $C_8H_6O_4$ and 0.024 mol NaOH were dissolved in a 300 ml deionized water under stirring. After that, 60 mL of a 0.25 M $CuSO_4$ aqueous solution was simultaneously added dropwise into the above solution under constant stirring. The mixture was stirred for 5 h at room temperature until MOF precipitation finished. The product was collected and washed with ethanol and deionized water for several times. At last, the white powder of Cu-MOF was dried in vacuum at 50 ℃.

Cu-MOF@SiO₂ preparation. 0.9 g Cu-MOF sample was dispersed in a mixture solution containing deionized water (180 g), ethanol (99 g), and ammonia solution (6.336 g). Subsequently, TEOS (6.75 mL) was added and stirred for 3 h at room temperature. Then, the

precipitation was collected and washed with ethanol and deionized water for several times, and air-dired at 80 ℃ for 5 h.

H-SCC synthesis. The Cu-MOF@SiO$_2$ composite was thermally treated at 700 ℃ for 5 h under argon atmosphere with a ramping rate of 5 ℃ min^{-1} and then naturally cooled down to room temperature. Finally, the product was taken out for battery preparation.

Characterization. The composite was characterized by X-ray diffraction (XRD) which was carried out using an AXS D8 Advance Diffractometer (Cu-Kα radiation, receiving slit 0.2 mm, scintillation counter, 40 mA, 40 kV) in the range of 2θ=10-90°. The microstructure and morphology of the as prepared composite were characterized using a Hitachi S-4800 field emission scanning electron microscope (SEM) and an FEI Tecnai G2 F20 transmission-electron microscopy (TEM) at an accelerating voltage of 200 kV. The BET specific surface area was analyzed using N$_2$ absorption using an ASAP 2020M (Micromeritics Instrument Corp., USA). FTIR measurements were carried out at room temperature using a NICOLET 6700 machine (Thermo Fisher Scientific, USA). In order to identify the content of SiO$_2$ of the composite, thermal gravimetric analysis (TGA) has been performed for the composite under air in a TGA machine (Pyris Diamond) employing at a heating rate of 10 K min^{-1}.

Electrochemical tests. To evaluate the electrochemical performance, the electrodes were fabricated using the mixture made up of 80 wt% active material, 10 wt% acetylene black and 10 wt% carboxymethyl cellulose (CMC). Lithium metal was used as the counter and reference electrode. The electrolyte was composed of a 1 mol L^{-1} LiPF$_6$ solution in fluoroethylene carbonate (FEC), dimethyl carbonate (DMC) and ethyl methyl carbonate (EMC) in 1:1:1 (v/v/v) ratio. 2032 Coin cells were assembled in a glove box filled with high-purity argon. The discharge-charge measurement of the cells was conducted on a LAND CT2000 battery test

system in a voltage range of 0.01-1.5 V (vs. Li^+/Li). The cyclic voltammetry experiments were carried out on a CHI660 Electrochemical Workstation (Shanghai Chenhua) in the potential window from 0.01 to 1.5 V (vs. Li^+/Li) at a scan rate of 0.05 mV s^{-1}. Electrochemical impedance spectroscopy (EIS) was carried out using a Solartron 1470E Electrochemical Interface (Solartron Analytical, UK) electrochemical workstation at 25℃ with the frequency ranging from 1 MHz to 0.01 Hz and AC signal of 10 mV in amplitude as the perturbation.

RESULTS AND DISCUSSION

The fabrication procedure of the H-SCC nanocomposite is shown in **Fig. 1**. First, Cu-MOF was synthesized using p-Phthalic acid, Copper sulfate pentahydrate, and sodium hydroxide as raw materials. Second, Cu-MOF was dispersed into ammonium hydroxide solution, and we could find that Cu-MOF was dissolved and the solution was clear, which we can observe in experiment. Then, TEOS was added into the solution, and the solution was muddy. After filtration, wash, and calcination, the H-SCC nanocomposite using Cu-MOF as a skeleton and TEOS as silicon source is synthesized. Due to the dispersion and dissolution of Cu-MOF, at last, the H-SCC is spherical. The reaction mechanism of the formation of the hollow structure is not clear, and it may be due to the induction of the Cu-MOF material, which is needed further study. XRD patterns of the H-SCC nanocomposite are shown in **Fig. 2a**. The H-SCC nanocomposite shows a broad peak at $2\theta = 21.8°$, which indicates an amorphous 002 silica phase. Furthermore, there are three more diffraction peaks, $2\theta = 43.6°$, $50.6°$, and $74.3°$, which can be readily indexed to the tetragonal phase Cu (JCPDS no.: 65-9743) due to the use of $CuSO_4•5H_2O$ during the preparation process. **Fig. S1** shows XRD patterns of the prepared Cu-MOF composite. The TGA curve obtained from the sample is shown in **Fig. 2b**. From the curve of the H-SCC nanocomposite, we can calculate that the weight of SiO_2 and ultrafine Cu nanoparticles in the

nanocomposite is about 95.11%. **Fig. 2c** is the FTIR spectra of the H-SCC nanocomposite. There

are three characteristic peaks around 1102, 800, and 473 cm^{-1} attributed to SiO_2, which can be

assigned to asymmetry Si-O-Si bond stretching, SiO_4 tetrahedron ring, and Si-O-Si bond

deformation, respectively[16]. **Fig. 2d** shows the nitrogen adsorption-desorption isotherms of the

H-SCC nanocomposite, and the BET specific surface area of the composite is 14.01 m^2 g^{-1}. And

the pore size distribution of the H-SCC composite (Fig. S2) displays a pore volume of 0.0259

cm^3 g^{-1}, and possess two mesopores (peaks at 2.0 and 10.2 nm) corresponding to the

decomposition of the Cu-MOF and one macropore (peak at after 100 nm) related to adsorption

cumulative volume of the composite. X-ray photoelectron spectroscopy (XPS) of the H-SCC

composite (Fig. S6) indicates the presence of Si and SiO_2, and the shoulders at about 104 eV for

the H-SCC composite are indicative of the formation of SiO_x with x<2.[37]

As shown in **Fig. 3a**, the as synthesized Cu-MOF composite is rod-like with coarse surface,

which may be beneficial to the adsorption of SiO_2 nanoparticles. **Fig. 3b** and **Fig. S3** shows

representative images for the product. It is obvious that the as-synthesized H-SCC nanoparticles

with an average diameter of ~200 nm tends to huddle together after the heat treatment. From the

images, we can speculate that due to the MOF skeleton the SiO_2 nanoparticles tend to huddle

together, and due to the structural collapse of the MOF skeleton after the carbonization there are

void spaces in the composite, which can not only prevent the nanoparticles peeling off from the

current collector, but also alleviate the volume change, leading to enhanced cycle life of the

batteries. More detailed morphologies and structure were determined by TEM and HRTEM.

TEM images demonstrate the hollow structure of the silica nanospheres (**Fig. 3c, d**), the shell of

which shows a thickness of about 50 nm. The composite is presented as a hollow structure with

the silica-copper-carbon shell and the void space core. The generated hollow structure can

accommodate the volume change during the lithiation/delithiation process, thus benefit the electrochemical performance. The H-SCC nanoparticles also tend to huddle together. **Fig. 3e** shows the energy dispersive spectroscopy (EDS). The EDS patterns reveal no other impurity peaks besides Si, O, C and Cu (**Table. S1**). The corresponding HRTEM image (**Fig. 3f**) shows the particle size of Cu is uniform about ~5 nm and embedded in the amorphous SiO_2 matrices, which is in accordance with XRD measurement and consists of amorphous SiO_2 and crystalline Cu. **Fig. 3g** is an SAED (selected area electron diffraction) pattern of the H-SCC nanocomposite, in which some halo diffraction rings can be observed, demonstrating the amorphous structure of silica and the rings with some discrete spots corresponding to the polycrystalline nature of ultrafine Cu nanoparticles. This is consistent with the phase established by XRD characterization. Combined with the dark field scanning TEM (STEM) images (**Fig. 3h**), elemental mappings of the Si, O, Cu, and C in the composite demonstrate a homogeneous distribution of the H-SCC nanocomposite. It is anticipated that the uniformly distributed copper and carbon not only enhance the electrical conductivity of the nanocomposite, but also accommodate the large volume change during the lithiation/delithiation process, resulting in good electrochemical performance in LIBs electrode.

The charge-discharge profiles of the H-SCC nanocomposite are shown in **Fig. 4a**. The first Li insertion and extraction capacities of the H-SCC anode are 1222.3 mA h g^{-1} and 564.4 mA h g^{-1}, respectively, corresponding to an initial coulombic efficiency of 46.2%. The irreversible capacity during the first cycle is caused by the formation of solid electrode interface (SEI) layer and also by the formation of the electrochemically inactive materials. The electrochemical reactions of SiO_2 can be expressed as follows:

$$SiO_2 + 4Li^+ + 4e^- \rightarrow 2Li_2O + Si \tag{1}$$

$$2SiO_2 + 4Li^+ + 4e^- \rightarrow Li_4SiO_4 + Si \tag{2}$$

8

$$Si+xLi^+ + xe^- \leftrightarrow Li_xSi \tag{3}$$

The first two reactions are irreversible with the formation of irreversible Li_2O and lithium silicate. After the first cycle, the electrochemical reaction of the electrode is reversible based on reaction 3. The charge/discharge capacities slightly increase in the subsequent cycles, which may be attributed to the activation of active materials. The electrochemical behavior of the H-SCC nanocomposite is further studied by cyclic voltammogram (CV) in a potential window of 0.01-1.5 V (vs. Li^+/Li) at a scanning rate of 0.05 mV s^{-1} for the first 8 cycles, as shown in **Fig. 4b**. In the first half-cycle, a broad cathodic peak at around 0.87 V could be ascribed to the formation of a SEI film, that is the decomposition of electrolyte.[38-41] This peak disappears under the subsequent cycles, which shows that no new SEI film forms. The following peak occurring at 0.2 V can be attributed to the irreversible formation of Li_2O and lithium silicate as well as lithiation of Si. In the case of the first anodic process, a broader anodic peak at 0.5 V corresponds to the extraction of lithium ion from Li-Si alloys. CV behavior presents slightly increase after the first cycle, demonstrating that the H-SCC nanocomposite becomes activated during the initial cycles, which is in good agreement with the charge-discharge profiles in **Fig. 4a**. The cycle stability and the coulombic efficiency of the H-SCC nanocomposite at a current density of 50 mA g^{-1} are shown in **Fig. 4c**. The initial charge capacity of the H-SCC nanocomposite is 564.4 mA h g^{-1}. Upon cycling, the capacity slightly increases and then stabilizes at a reversible capacity of 766.1 mA h g^{-1}. The rate capability of the electrode is tested at different current densities from 50 mA g^{-1} to 5000 mA g^{-1}, as shown in **Fig. 4d**, demonstrating capacity recovery ability of the H-SCC nanocomposite.

The cycle performance of the H-SCC nanocomposite at 500 mA g^{-1} between 0.01 and 1.5 V vs. Li^+/Li is investigated, as shown in **Fig. 4e**. The rate was 50 mA g^{-1} for the first 3 cycles and 500 mA/g for the later cycles. From the 4th to 400th cycle at 500 mA g^{-1}, the capacity retention

was more than 99.5%. After 400 cycles, over 492 mA h g^{-1} capacity retained, which is larger than the theoretical capacity of graphite. After the first several cycles, the coulombic efficiency could increase and stabilize at 99.6% in subsequent cycles. The electrochemical performance of the H-SCC nanocomposite is superior to that previously reported 560 mA h g^{-1} at 50 mA g^{-1} for unique porous carbon/silica composite[16], 500 mA h g^{-1} after 50 cycles for carbon-coated SiO_2 nanoparticles[17], 567 mA h g^{-1} at 50 mA g^{-1} for electrospun PAN/SiO_2 composite nanofiber[18]. This suggests that the H-SCC nanocomposite is a promising material anode for LIBs. The long cycling stability and rate capability of the H-SCC electrode are ascribed to the hollow structure and the carbonized Cu-MOF skeleton. The free volume in the composite, such as hollow structure and the structure collapse of the MOF skeleton, can accommodate the huge volume change and buffer the mechanical stress. The carbon from the decomposition of the MOF skeleton can not only enhance the electrical conductivity of the composite and preserve the structural and interfacial stabilization, but also suppress the aggregation of silica nanoparticles and buffer the volume change. What's more, the ultrafine copper nanoparticles with homogeneous distribution in SiO_2 matrices, which look like seeds of the pitaya fruit, have many functions during charge/discharge processes, such as improving the electrical conductivity of the active material and buffering the mechanical stress and enhancing the rate capability of the composite.

Electrochemical impedance spectroscopy (EIS) of the H-SCC electrode is investigated to gain further insights into the rate capability and the cycling performance (**Fig. 5a**). The frequency range is set between 1 MHz and 0.01 Hz, and EIS is carried out on the samples after being charged to 1.5 V at 0.05 C in the 1th, 2th, 5th, 100th cycle, respectively. The Nyquist plots show a depressed semicircle at high frequency and a straight line at low frequency. The diameter of the

depressed semicircle represents the resistance of the charge-transfer process, while the straight line corresponds to the diffusion of lithium ion in the H-SCC electrode. After the 1st, 2nd, 5th, 100th cycle, the spectra have the similar features: one relatively stable diameter of depressed semicircle at high frequency and a straight line at low frequency, which indicates a good interfacial stabilization between the current collector and the H-SCC electrode. In order to investigate the effect of cycling on the morphology of the H-SCC nanocomposite, the half cells were disassembled in a charged state after 400 cycles for SEM analysis. **Fig. 5b** and **5c** shows there are no obvious morphology change in contrast to **Fig. 3b**, except that the average diameter of the composite appeared a little increase due to the formation of SEI film and the volume change. The structure of the electrode keeps integrity. **Fig. 5d** shows the schematic of structure evolution of the H-SCC nanocomposite before and after electrochemical cycling. The hollow structure[42, 43] allowed the H-SCC nanocomposite to expand freely without fracture and mechanical failure during lithiation/delithiation processes, in which the Cu and C materials in the matrices can also cushion the volume change as well as prevent the composite aggregation.

The superior electrochemical performance of the H-SCC nanocomposite could be ascribed to its unique nanostructure: the MOF skeleton after carbonization is believed to provide conductive network, which can not only facilitate Li^+ and electron transport, but also buffer the volume change of SiO_2 as well as prevent the SiO_2 nanoparticles aggregation. The ultrafine copper nanoparticles with homogeneous distribution in SiO_2 matrices have many functions during charge/discharge processes, such as improving the electrical conductivity of the active material and buffering the mechanical stress and enhancing the rate capability of the composite. The void space resulting from the carbonization of the MOF skeleton is beneficial to increase the surface area accessible to the electrolyte and can further cushion the volume change of SiO_2 during

alloying/dealloying process. Moreover, the hollow structure of the composite can buffer the huge volume change and reduce the diffusion-induced stress, leading to a structural integrity to have a good electrochemical performance.

Conclusions

In summary, for the first time, we fabricate a novel material of the H-SCC nanocomposite using MOF as skeleton. The as-synthesized composite exhibits good electrochemical performance. The reversible capacity is around 500 mA h g^{-1} at a current density of 500 mA g^{-1} after 400 cycles, much higher than that of the previously reported SiO$_2$/C composites. This good electrochemical performance is ascribed to the carbonized Cu-MOF skeleton. The void space results from the carbonization of the MOF skeleton and the hollow structure of silica, which can provide conductive network, can buffer the volume change to prevent the aggregation. The uniform distribution of the ultrafine copper and carbon in SiO$_2$ matrices can also alleviate mechanical stress during lithiation process and provide enhanced electrical conductivity. It gives an opportunity for the large-scale application of H-SCC nanocomposite as an anode in LIBs through the low-cost and facile fabrication process.

Acknowledgements

References:

1.   V. Etacheri, R. Marom, R. Elazari, G. Salitra and D. Aurbach, Energy & Environmental Science, 2011, 4, 3243-3262.

2.   Z. Yang, J. Zhang, M. C. W. Kintner-Meyer, X. Lu, D. Choi, J. P. Lemmon and J. Liu, Chemical Reviews, 2011, 111, 3577-3613.

3.   J. B. Goodenough and K.-S. Park, Journal of the American Chemical Society, 2013, 135, 1167-1176.

4.   F. Xin, X. Wang, J. Bai, W. Wen, H. Tian, C. Wang and W. Han, Journal of Materials Chemistry A, 2015, 3, 7170-7178.

5.   V. Etacheri, R. Marom, R. Elazari, G. Salitra and D. Aurbach, Energy & Environmental Science, 2011, 4, 3243.

6.   J. Chang, X. Huang, G. Zhou, S. Cui, P. B. Hallac, J. Jiang, P. T. Hurley and J. Chen, Advanced Materials, 2014, 26, 758-764.

7.   D. M. Piper, J. H. Woo, S.-B. Son, S. C. Kim, K. H. Oh and S.-H. Lee, Advanced Materials, 2014, 26, 3520-3525.

8.   R. Zhang, Y. Du, D. Li, D. Shen, J. Yang, Z. Guo, H. K. Liu, A. A. Elzatahry and D. Zhao, Advanced Materials, 2014, 26, 6749-6755.

9.   L. Pan, H. Wang, D. Gao, S. Chen, L. Tan and L. Li, Chemical Communications, 2014, 50, 5878.

10.   M. W. Forney, M. J. Ganter, J. W. Staub, R. D. Ridgley and B. J. Landi, Nano letters, 2013, 13, 4158-4163.

11.   J. Liu, N. Li, M. D. Goodman, H. G. Zhang, E. S. Epstein, B. Huang, Z. Pan, J. Kim, J. H. Choi, X. Huang, J. Liu, K. J. Hsia, S. J. Dillon and P. V. Braun, ACS Nano, 2015, 9, 1985-1994.

12.   T. D. Bogart, D. Oka, X. Lu, M. Gu, C. Wang and B. A. Korgel, ACS Nano, 2014, 8, 915-922.

13.   H. Tian, X. Tan, F. Xin, C. Wang and W. Han, Nano Energy, 2015, 11, 490-499.

14.   M. Li, Y. Yu, J. Li, B. Chen, X. Wu, Y. Tian and P. Chen, J. Mater. Chem. A, 2015, 3, 1476-1482.

15.   R. B. Cervera, N. Suzuki, T. Ohnishi, M. Osada, K. Mitsuishi, T. Kambara and K. Takada, Energy Environ. Sci., 2014, 7, 662-666.

16.   X. Yang, H. Huang, Z. Li, M. Zhong, G. Zhang and D. Wu, Carbon, 2014, 77, 275-280.

17.   Y. Yao, J. Zhang, L. Xue, T. Huang and A. Yu, Journal of Power Sources, 2011, 196, 10240-10243.

18.   L. Ji, Z. Lin, A. J. Medford and X. Zhang, Carbon, 2009, 47, 3346-3354.

19.   M. Au, Y. He, Y. Zhao, H. Ghassemi, R. S. Yassar, B. Garcia-Diaz and T. Adams, Journal of Power Sources, 2011, 196, 9640-9647.

20.   H. Guan, X. Wang, S. Chen, Y. Bando and D. Golberg, Chemical communications, 2011, 47, 12098-12100.

21.   G. Li, Y. Song, L. Zhang, X. I. N. Wei, X. Song and Z. Sun, Functional Materials Letters, 2013, 06, 1350033.

22.   D. B. Polat, O. Keles and K. Amine, Journal of Power Sources, 2014, 270, 238-247.

23.   J. Qu, H. Li, J. J. Henry, S. K. Martha, N. J. Dudney, H. Xu, M. Chi, M. J. Lance, S. M. Mahurin, T. M. Besmann and S. Dai, Journal of Power Sources, 2012, 198, 312-317.

24.   V. A. Sethuraman, K. Kowolik and V. Srinivasan, Journal of Power Sources, 2011, 196, 393-398.

25.   L. Sun, X. Wang, R. A. Susantyoko and Q. Zhang, Journal of Materials Chemistry A,

2014, 2, 15294.

26.   H. Wu, N. Du, H. Zhang and D. Yang, J. Mater. Chem. A, 2014, 2, 20510-20514.

27.   Z. Yang, D. Wang, F. Li, H. Yue, D. Liu, X. Li, L. Qiao and D. He, Materials Letters, 2014, 117, 58-61.

28.   P. Zuo, G. Yin, X. Hao, Z. Yang, Y. Ma and Z. Gao, Materials Chemistry and Physics, 2007, 104, 444-447.

29.   M. Li, Z. Yu and M. Qu, Journal of Alloys and Compounds, 2010, 491, 643-648.

30.   A. Morozan and F. Jaouen, Energy & Environmental Science, 2012, 5, 9269.

31.   J.-K. Sun and Q. Xu, Energy & Environmental Science, 2014, 7, 2071.

32.   R. Wu, X. Qian, F. Yu, H. Liu, K. Zhou, J. Wei and Y. Huang, Journal of Materials Chemistry A, 2013, 1, 11126.

33.   R. R. Salunkhe, Y. Kamachi, N. L. Torad, S. M. Hwang, Z. Sun, S. X. Dou, J. H. Kim and Y. Yamauchi, J. Mater. Chem. A, 2014, 2, 19848-19854.

34.   Y. Lü, W. Zhan, Y. He, Y. Wang, X. Kong, Q. Kuang, Z. Xie and L. Zheng, ACS Applied Materials & Interfaces, 2014, 6, 4186-4195.

35.   R. Wu, X. Qian, K. Zhou, J. Wei, J. Lou and P. M. Ajayan, ACS Nano, 2014, 8, 6297-6303.

36.   X. Xu, R. Cao, S. Jeong and J. Cho, Nano Letters, 2012, 12, 4988-4991.

37.   H. Kim, M. Seo, M. H. Park and J. Cho, Angewandte Chemie, 2010, 49, 2146-2149.

38.   Y. Chen, Q. Z. Huang, J. Wang, Q. Wang and J. M. Xue, Journal of Materials Chemistry, 2011, 21, 17448-17453.

39.   S. Li, W. Xie, S. Wang, X. Jiang, S. Peng and D. He, Journal of Materials Chemistry A, 2014, 2, 17139-17145.

40. A. Bhaskar, M. Deepa and T. N. Rao, Nanoscale, 2014, 6, 10762-10771.

41. Y. Zhao, J. Li, Y. Ding and L. Guan, RSC Advances, 2011, 1, 852-856.

42. S. Chen, M. L. Gordin, R. Yi, G. Howlett, H. Sohn and D. Wang, Physical Chemistry Chemical Physics, 2012, 14, 12741-12745.

43. J. Ryu, S. Choi, T. Bok and S. Park, Nanoscale, 2015, 7, 6126-6135.

Figure and scheme captions
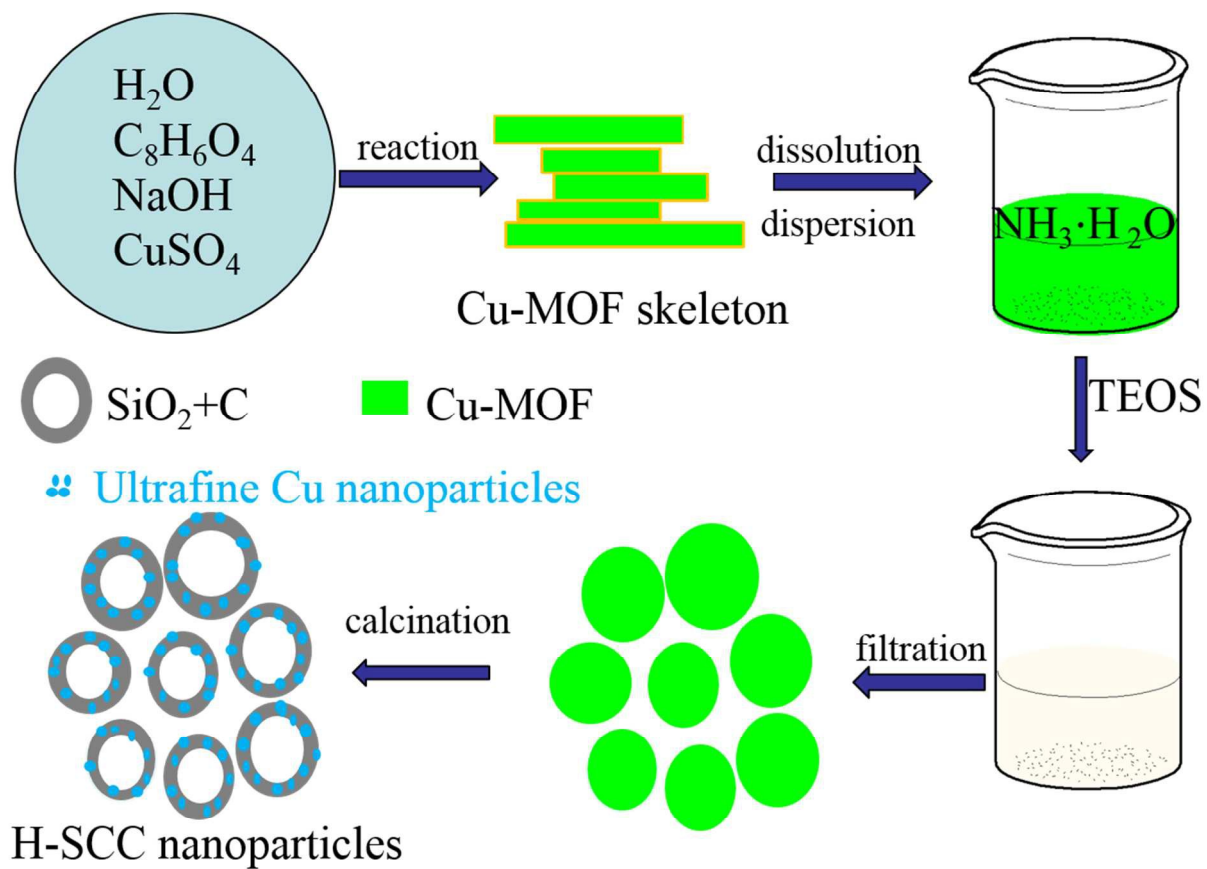
Fig. 1 Schematic illusion of the formation of the H-SCC nanocomposite.
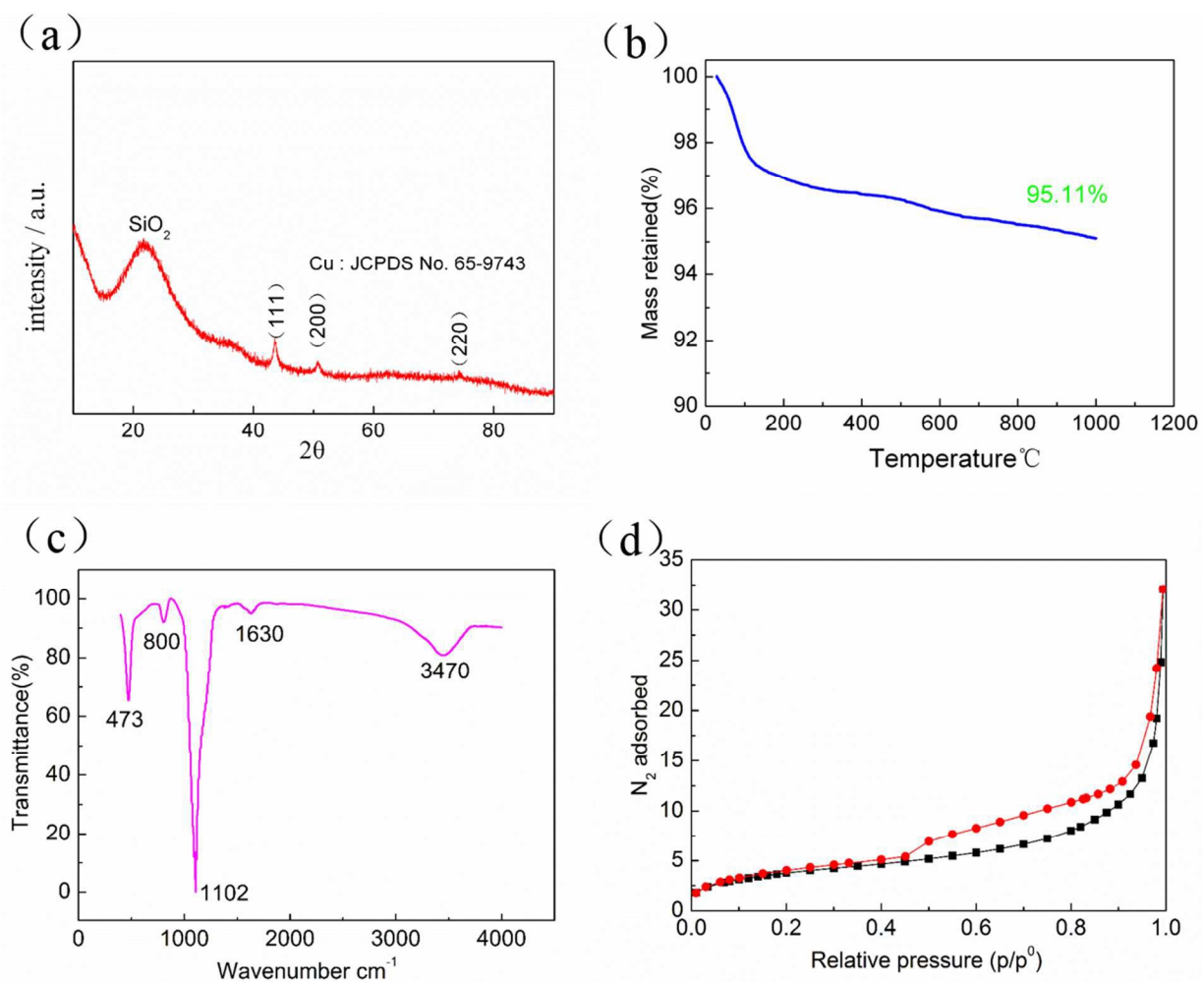
Fig. 2 (a) XRD patterns of the as-synthesized H-SCC nanocomposite. (b) TGA curve under air atmosphere with a rate of 10 ℃ min^{-1}. (c) FTIR spectroscopy of the as-synthesized H-SCC nanocomposite. (d) Nitrogen adsorption-desorption isotherm curve of the H-SCC nanocomposite.
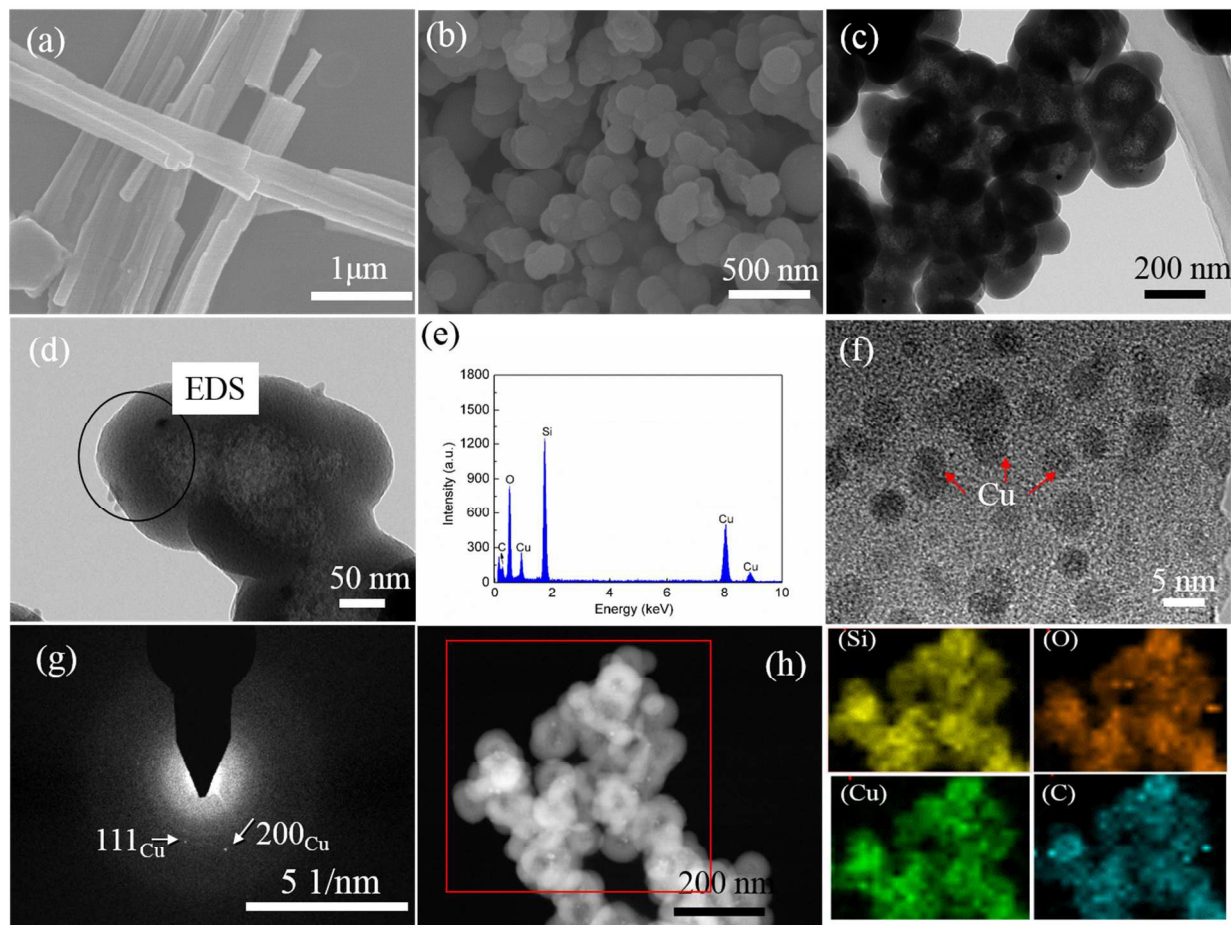
Fig. 3 (a) FESEM image of Cu-MOF. (b) FESEM image of products obtained after heating Cu-MOF@SiO$_2$ at 700℃. (c) Low- and (d) high-magnified TEM images of the obtained H-SCC nanocomposite. (e) EDS profile. (f) High-resolution TEM image. (g) The SAED pattern. (h) TEM image and elemental mapping images of the H-SCC nanoparticles.
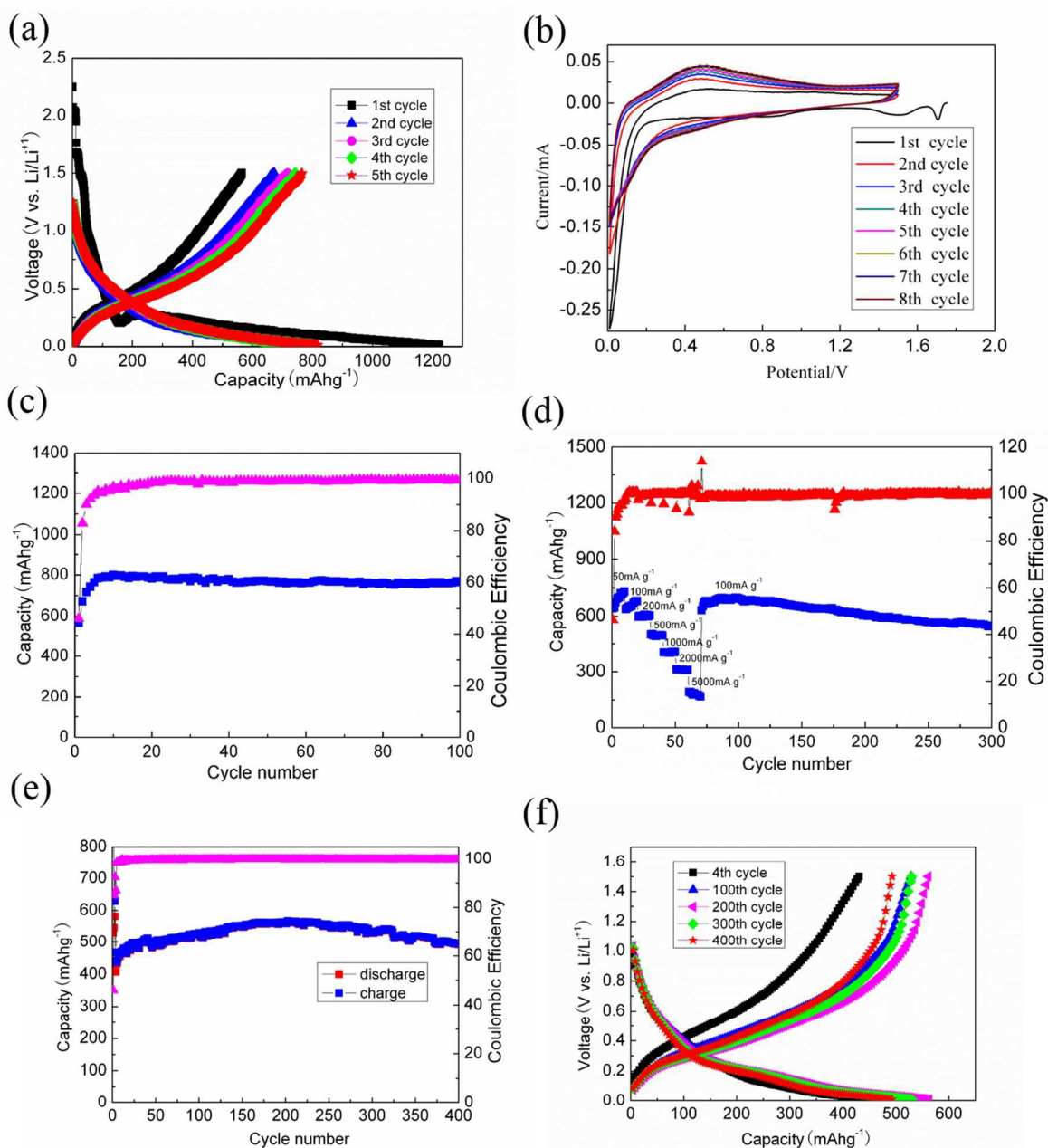
Fig. 4 (a) Galvanostatic charge/discharge profiles of the H-SCC anode at a current density of 50 mA g^{-1}. (b) Cyclic voltammogram of the 1st to 8th cycle of the as-prepared H-SCC nanocomposite between 0.01 to 1.5 V (vs. Li$^+$/Li) at a scanning rate of 0.05 mV s^{-1}. (c) Cycling performance of the H-SCC electrode at a current density of 50 mA g^{-1}. (d) Rate capability of the H-SCC nanocomposite at different discharge currents. (e) Cycling performance of the H-SCC electrode at a current density of 500 mA g^{-1}. (f) Galvanostatic charge/discharge profiles of the H-SCC anode at a current density of 500 mA g^{-1}.
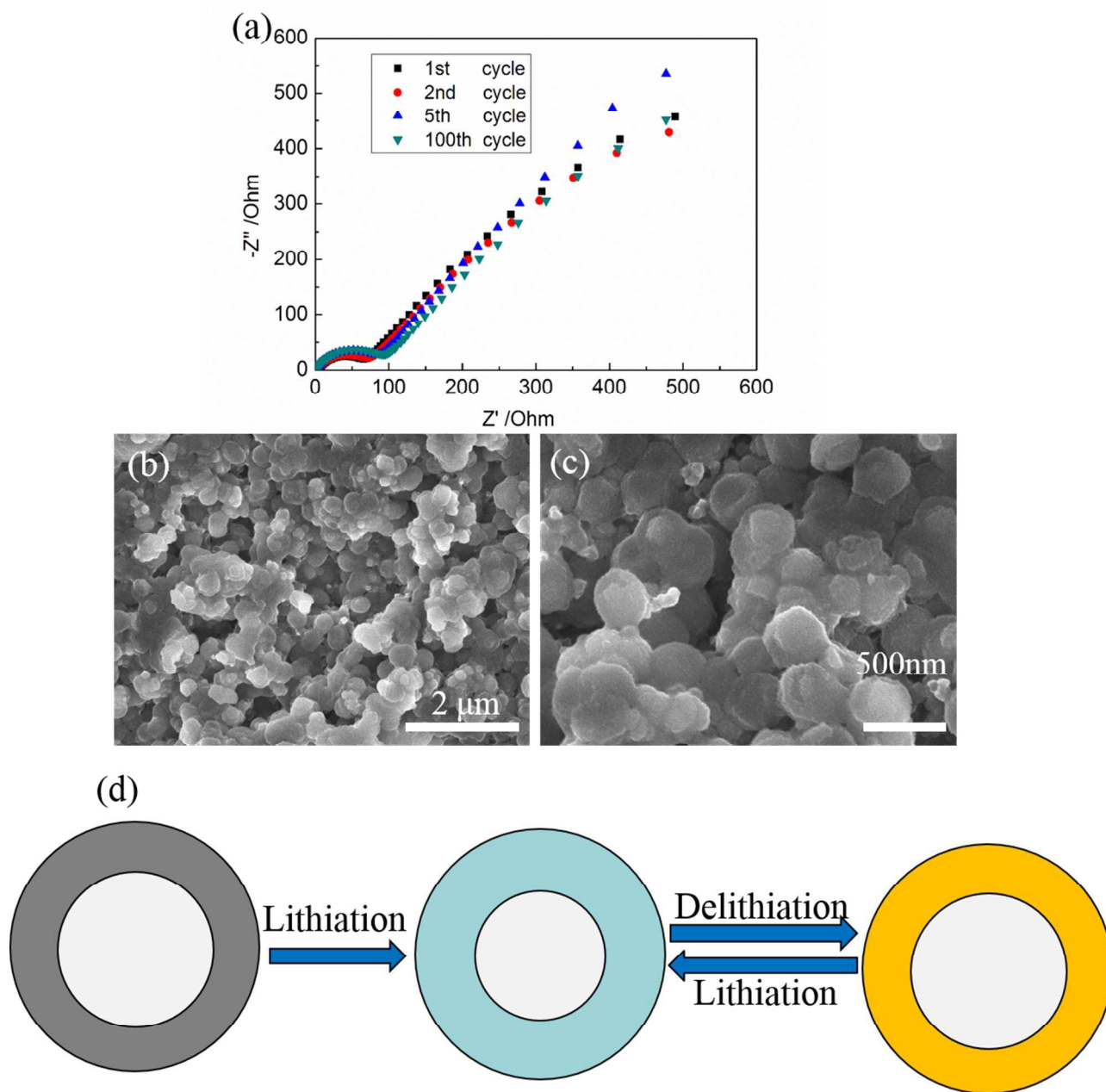
Fig. 5 (a) Nyquist plots of the electrodes of the H-SCC nanocomposite after 1, 2, 5 and 100 charge-discharge cycles at 50 mA g^{-1}, obtained after charging to 1.5 V. (b) Low- and (c) high-magnified FESEM images of the composite after 400 cycles at a current density of 500 mA g^{-1}. (d) Schematic of the H-SCC nanocomposite before and after electrochemical cycling.

Supporting information

Hollow silica-copper-carbon anodes using copper metal-organic frameworks as skeletons

Zixu Sun[†], Fengxia Xin[†], Can Cao[‡], Chongchong Zhao[†], Cai Shen[†], Wei-Qiang Han[†,*]

[†]Ningbo Institute of Materials Technology & Engineering, Chinese Academy of Sciences, Ningbo 315201, P. R. China

[‡]Department of Materials Science and Engineering, Zhejiang University, Hangzhou 310027, P. R. China

*Correspondence and requests for materials should be addressed to W.Q.H. *e-mail:*

hanweiqiang@nimte.ac.cn
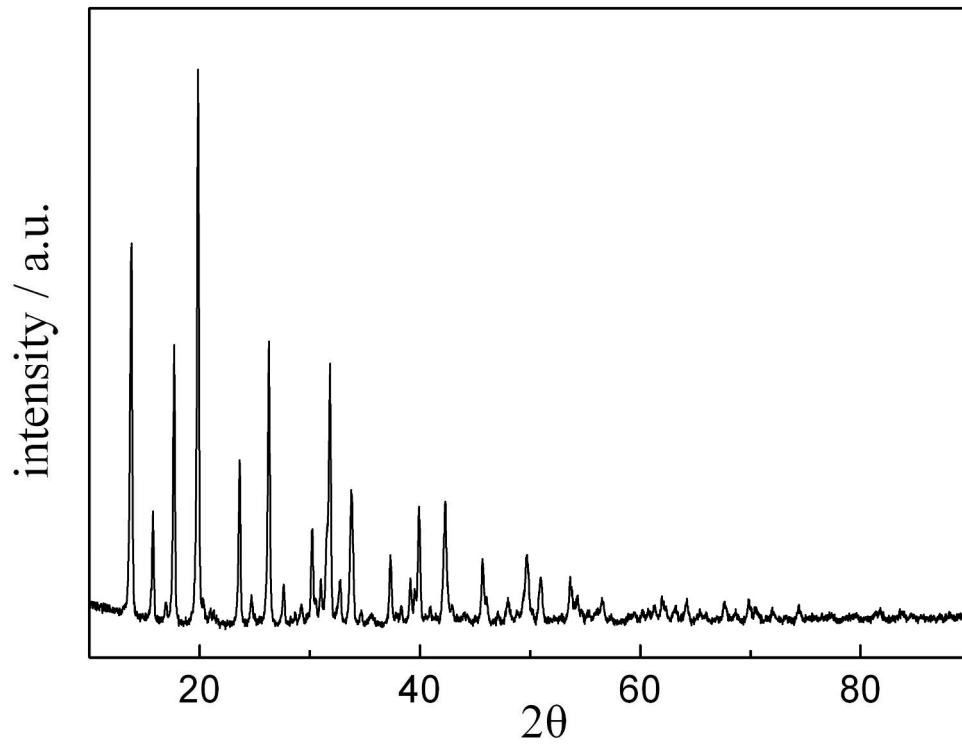
Fig. S1 XRD patterns of as-synthesized Cu-MOF template.
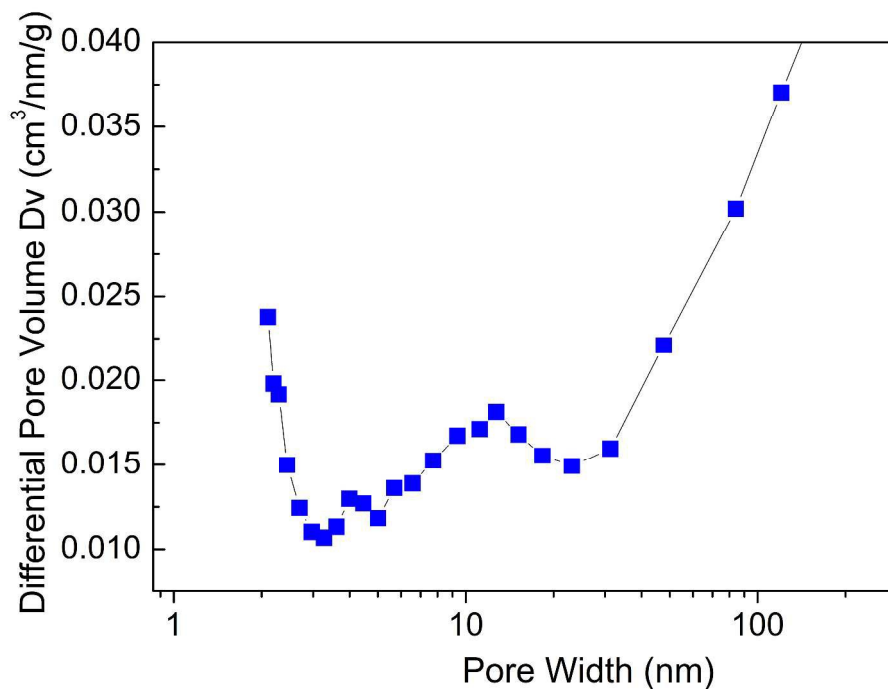
Fig. S2 pore size distribution of the H-SCC composite.
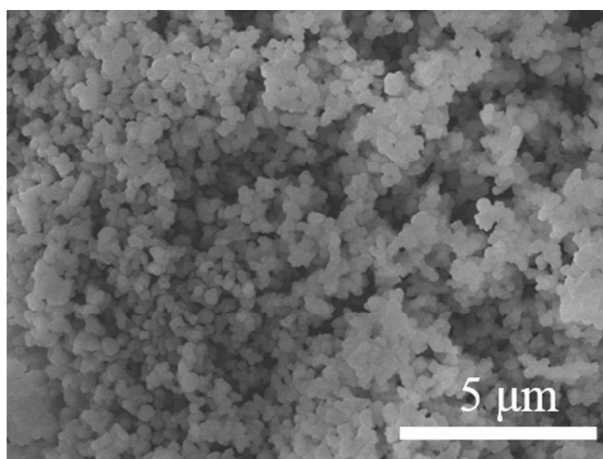
Fig. S3 Low-magnified FESEM image of products obtained after heating Cu-MOF@SiO$_2$ at

700 ℃.

Table. S1 the content of C, O, Si, Cu by the EDX.

Element	C (K)	O (K)	Si (K)	Cu (K)
Weight %	2.43	48.44	33.24	15.87
Atomic %	4.34	64.91	25.38	5.35
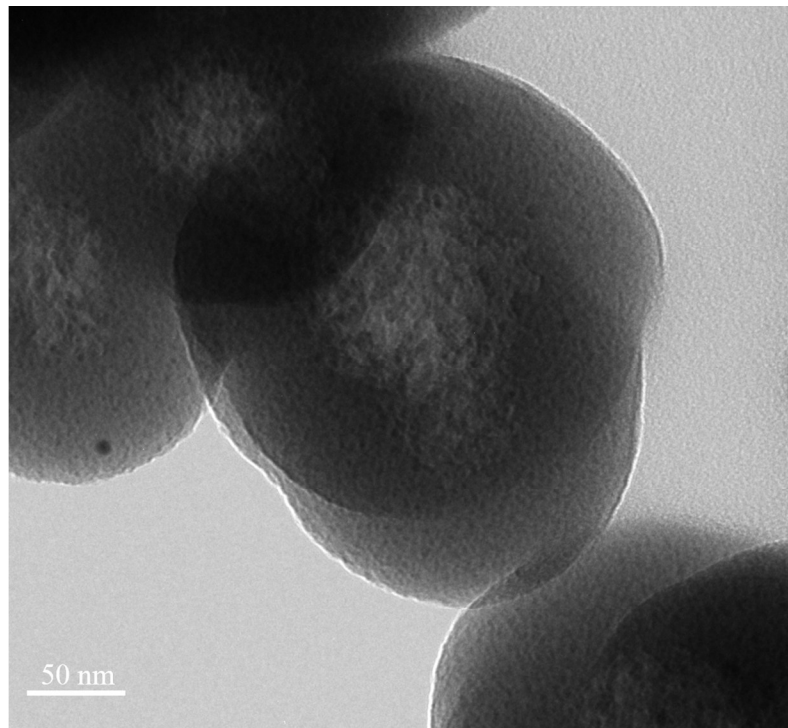
Fig. S4 higher resolution TEM image of the H-SCC nanocomposite.
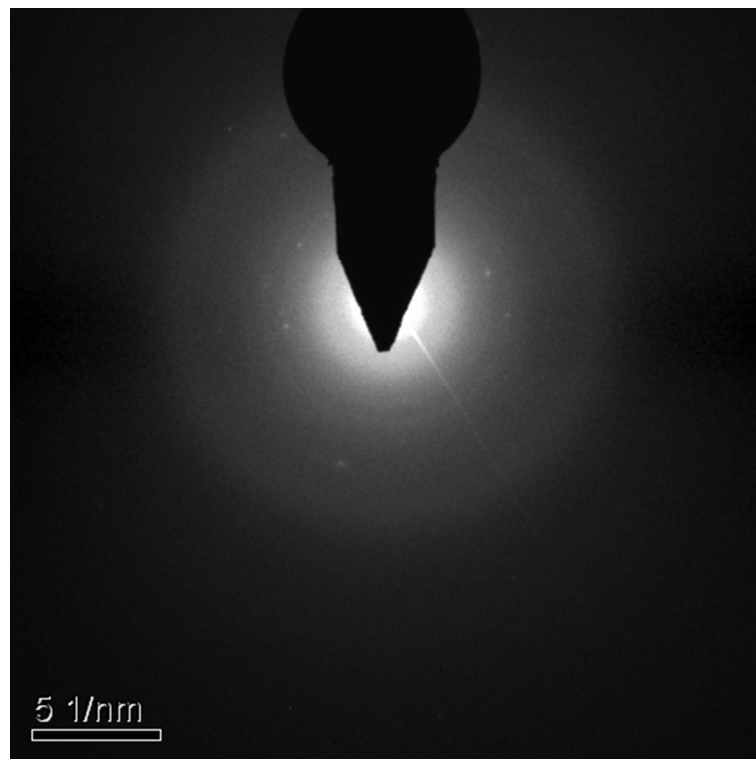
Fig. S5 the SAED pattern of the H-SCC composite.
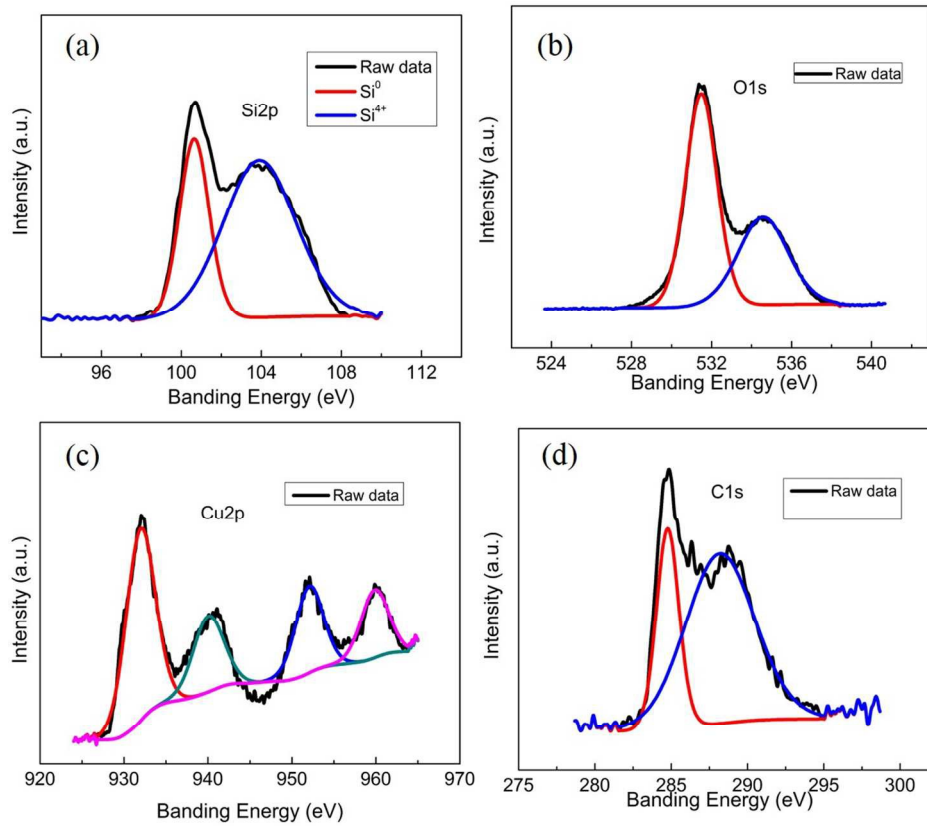
Fig. S6 XPS spectra for the H-SCC composite: (a) Si 2p; (b) O 1s; (c) Cu 2p; and (d) C1s.